

# Cyclic degradation and non-coaxiality of soft clay subjected to pure rotation of principal stress directions

Jian-Gu Qian<sup>1,2</sup> · Zi-Bo Du<sup>1,2</sup> · Zhen-Yu Yin<sup>1,2,3</sup>

Received: 7 August 2016 / Accepted: 30 May 2017 / Published online: 15 June 2017  
© Springer-Verlag GmbH Germany 2017

**Abstract** Foundation soils are often under non-proportional cyclic loadings. The deformation behaviour and the mechanism of non-coaxiality under continuous pure principal stress rotation for clays are not clearly investigated up to now. In order to study the effect of pure principal stress rotation, a series of cyclic undrained tests on Shanghai soft clay subjected to cyclic rotation of principal stress directions keeping the deviatoric stress constant under the pure rotation condition were conducted using hollow cylinder apparatus. Based on this, the evolutions of excess pore pressure and strains during cyclic loading were investigated, together with the effects of the intermediate principal stress parameter and the deviatoric stress level on stress–strain stiffness and non-coaxiality. The result can provide an experimental basis for constitutive modelling of clays describing the behaviour under non-proportional loadings.

**Keywords** Anisotropy · Clay · Cyclic loading · Intermediate principal stress · Non-coaxiality · Principal stress rotation

## 1 Introduction

Foundation soils during the construction or operation of geotechnical structures are often under complex loadings (e.g. wave loadings, earthquakes, and traffic loadings). These loadings result in continuous and cyclic principal stress rotation in soils, which is classified as non-proportional loading, and will cause non-coaxiality behaviour of soils compared to conventional proportional loading. In general, natural soils are inherently anisotropic. This inherent anisotropy highlights the fact that their response to loading will depend on the orientation of principal stress with the deposition direction. Experimental studies have indicated that cyclic rotation of principal stress directions is able to generate plastic strain, plastic compressed volumetric strain under drained conditions, or excess pore pressure under undrained conditions even up to liquefaction [1–4, 7, 15, 17, 18, 24, 25, 28, 30, 31, 35, 36]. Moreover, the cyclic rotation of principal stress directions will induce more prominent stiffness degradation than cyclic loading under a fixed principal stress direction [8].

Up to now, a relatively thorough understanding was implemented in granular soils under principal stress rotation, but not for clay. Actually, it is technologically difficult to perform non-proportional loading tests for soft clay, so the existing experiments were confined to proportional loading or fewer cycles, which resulted in incomplete understanding of the deformation behaviour and the mechanism of non-coaxiality under pure principal stress rotation.

Therefore, this paper focuses on the cyclic degradation and non-coaxiality of soft clay subjected to pure rotation of principal stress directions. For this purpose, a series of undrained tests are conducted on Shanghai soft clay subjected to cyclic principal stress rotation under varying

---

✉ Zhen-Yu Yin  
zhenyu.yin@gmail.com

<sup>1</sup> Department of Geotechnical Engineering, Tongji University, Shanghai 200092, China

<sup>2</sup> Key Laboratory of Geotechnical and Underground Engineering of Ministry of Education, Tongji University, Shanghai 200092, China

<sup>3</sup> Research Institute of Civil Engineering and Mechanics (GeM), UMR CNRS 6183, Ecole Centrale de Nantes, Nantes, France

intermediate principal stress parameter  $b$  ( $b = (\sigma_2 - \sigma_3) / (\sigma_1 - \sigma_3)$ ) and the magnitude of deviatoric stress  $q$  using a hollow cylinder apparatus. In addition, the anisotropic cyclic degradation and the non-coaxiality behaviours are also investigated.

## 2 Equipment and test program

### 2.1 Test equipment

The TJ-5 Hz hollow cylinder apparatus (HCA) testing equipment at Tongji University was used in this study to investigate the behaviour of soft clay. The hollow cylinder apparatus can apply normal stresses individually to a specimen, including vertical normal stress, inner and outer cell pressures and shear stress. By combining the normal stress and the shear stress, complicated stress path loading conditions can be simulated.

The HCA has four individual systems for the control of the axial load  $W$ , torque  $T$ , inner cell pressure  $P_i$  and outer cell pressure  $P_o$ , which can enable the control of axial stress  $\sigma_z$ , radial stress  $\sigma_r$ , circumferential stress  $\sigma_\theta$ , and shear stress  $\tau_{z\theta}$ , respectively (Fig. 1). They are conveniently converted into an equivalent set of four stress-related parameters,  $p$ ,  $q$ ,  $b$ , and  $\alpha_\sigma$  (the angle between the major principal stress direction and the deposition direction,  $\alpha_\sigma = \arctan[2\tau_{z\theta} / (\sigma_z - \sigma_\theta)] / 2$ ). Two individually hydraulic control devices are responsible for regulating the inner and outer cell pressures, which are measured by hydraulic pressure transducers. The axial and torsional loads are generated by two mechanical–electronic servo control systems and recorded by the internal load cell, respectively. The corresponding axial displacement and rotation angle are measured accordingly when the servo-actuator is in the position control mode and read by digital

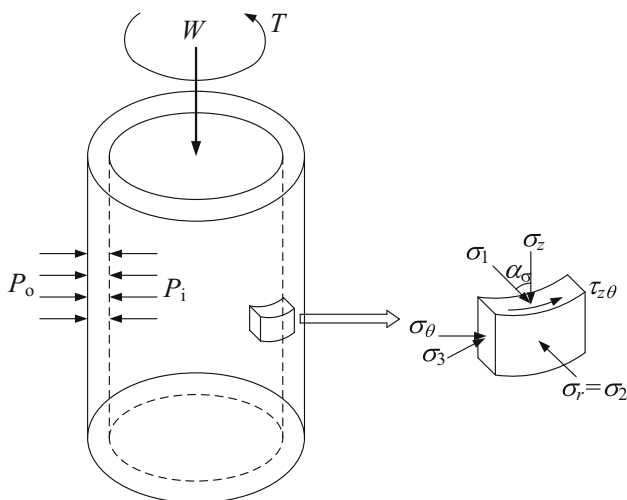


**Fig. 1** Stress state of soil element in hollow cylinder apparatus

control systems. The excess pore pressure is monitored by a pore pressure cell, such that the effective stress can be calculated.

The sample size used in the TJ-5 Hz HCA is as follows: outer radii  $r_o = 50$  mm, inner radii  $r_i = 30$  mm, and height  $H = 200$  mm.

### 2.2 Sample preparation

The soil used in this study for the sample preparation was obtained from a deep excavation site in Shanghai at a depth of 18–20 m. The physical properties of the tested clay are shown in Table 1. A conventional oedometer test on the undisturbed sample was carried out, as shown in Fig. 2, from which the preconsolidation pressure  $\sigma_p$  was determined to be 149 kPa.

All samples were trimmed to the specified outer diameter from top to bottom with a wire saw in a rotary manner in a sample preparation platform. Hollow cylinder samples were then formed by placing the soil cylinders in a metal mould with a height of the required sample size and cutting the cylinders by a special drill bit which has a radius of 30 mm spirally at the bottom of the centre from bottom to top. The cutting depth in each spin is no more than 1 cm, and the drill bit is rotated slowly about 1 cycle per minute to ensure the inner surface stable. The removed clay in each spin was dropped off under the action of gravity with some attached to the drill bit. The process was repeated until the desired inner diameter was achieved. For some drier samples, surface smoothness by careful fine trimming using the side of a blade was needed to prevent the non-uniformity caused by the friction between the inner clay surface and the drill bit. Finally, the sample was trimmed to the specified height with a wire saw along the metal mould. During the whole preparation, the inner wall is fully observed through a camera connected to the computer to ensure the quality of the inner wall.

### 2.3 Test program

Based on the study of Hight [11], the stress and strain components in HCA depend on the thin-wall assumption detailed in Table 3 in Appendix.

A back pressure of 50 kPa was applied, and the degree of saturation of all hollow cylinder specimens was examined by  $B$  values exceeding 0.96. Subsequently, all samples were isotropically consolidated to a mean effective stress of 150 kPa. Then, the designed stress path was automatically conducted through four independently controlled loads. Figure 3 shows the deviatoric stress path in the stress plane of  $\tau_{z\theta} - (\sigma_z - \sigma_\theta) / 2$ .

To investigate the inherent anisotropy of soft clay, two groups of undrained tests were carried out in this study.

**Table 1** Physical properties of Shanghai soft clay

Natural water content $w_n$ (%)	Plasticity index $I_p$	Liquidity index $I_L$	Specific gravity $G_s$	Initial void ratio $e_0$
38.4	18.2	0.99	2.75	1.060

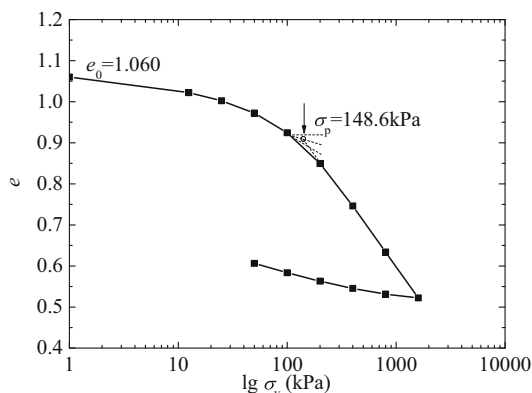


**Fig. 2** Compression curve in  $e$ - $\log \sigma_v$  from odometer test

The first test group was under monotonic loadings by increasing the deviatoric stress  $q$  monotonically up to failure, whereas the major principal stress inclination  $\alpha_\sigma$  was fixed at a specific angle, a mean total stress  $p$  and an intermediate principal stress parameter  $b$  kept constant, as shown in Fig. 3a. The second test group was under pure principal stress rotation, as shown in Fig. 3b, where the magnitude of deviatoric stress was first increased to a specific value (point B) under the drained condition, and then, the specimens were anisotropically consolidated, maintaining the constant stress ratio at a desired stress state. Subsequently, the shearing stage involving pure rotation of the major principal stress direction (B-C-D-E-B) was commenced under undrained condition. The  $p$ ,  $b$ , and  $q$  and the total principal stresses  $\sigma_1$ ,  $\sigma_2$ , and  $\sigma_3$  were maintained constant, whereas only the directions of the

principal stresses were continuously rotated during the pure rotation tests.

In general, the stress path given in Fig. 3b with principal stress rotation is defined as non-proportional loading used to simulate cyclic loading induced by wave loadings based mainly on Ishihara [14]. In the pure rotation tests, the torque was applied with an angular displacement rate of  $0.2^\circ/\text{min}$  to reduce the effect of the excess pore pressure hysteresis according to Akagi and Saitoh [1]. Akagi and Saitoh [1] and Zhou et al. [36] conducted similar tests on Tokyo clay and Hangzhou clay, respectively, using the same loading rate with excess pore water pressure equilibrium in sample during loading. Since the tested Shanghai clay is a silty clay with even a little bit higher permeability than Tokyo and Hangzhou clays, the selected rate should more easily make the equilibrium of excess pore water pressure in clay samples. This equilibrium was further confirmed by conducting a test at the loading rate of  $0.3^\circ/\text{minute}$ , in which almost identical excess pore pressure was measured, compared to the test at the rate of  $0.2^\circ/\text{minute}$ .

All tests were performed under the same initial mean effective stress of  $p' = 150 \text{ kPa}$  which is slightly bigger than the preconsolidation pressure  $\sigma_p$  to make sure the tested clay is normally consolidated. According to previous tests on permanent deformation responses of shanghai clay subjected to loadings with principal stress rotation [20], the clay shows cyclic stability (shakedown) under lower cyclic stress ratio (less than 0.25) but tends to cyclic plastic deformations up to failure under higher cyclic stress ratio (more than 0.30). Since the tested clay was taken from the

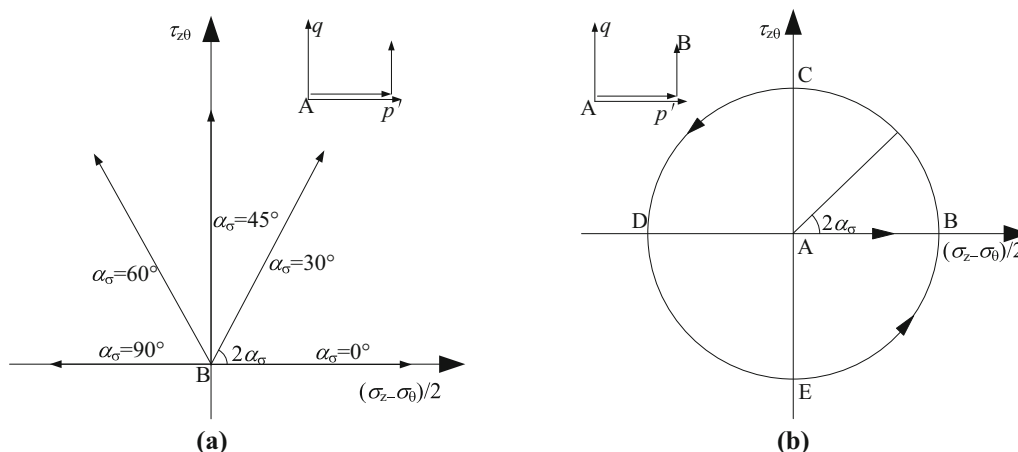


**Fig. 3** Stress path in deviatoric stress space: **a** monotonic loading; **b** pure rotation of principal stress directions

**Table 2** Test program

Test number	$P'$ (kPa)	$Q$ (kPa)	$B$	$\alpha_\sigma$ (°)/cycle numbers
Series I				
MF00-1	150	Failure	0.5	0
MF30-1	150	Failure	0.5	30
MF45-1	150	Failure	0.5	45
MF60-1	150	Failure	0.5	60
MF90-1	150	Failure	0.5	90
Series II				
RL00-2	150	30	0	0~1260/7
RL05-2	150	30	0.5	0~1260/7
RL10-2	150	30	1.0	0~1260/7
Series III				
RH00-3	150	60	0	0~720/4
RH05-3	150	60	0.5	0~720/4
RH10-3	150	60	1.0	0~720/4

same location with 2 m deeper, two cyclic stress ratios were determined with the lower and higher cyclic stress ratio 0.2 and 0.4, respectively.

As mentioned in introduction, since the paper mainly focuses on the stress–strain characteristics, such as cyclic degradation and non-coaxiality, only several cycles were applied during which the excess pore pressure is mainly developed. In total, 11 undrained tests were conducted under various conditions. According to the stress paths and applied deviatoric stress levels, all tests were divided into three series, as listed in Table 2.

### 3 Test results and discussion

#### 3.1 Strength anisotropy of undisturbed Shanghai soft clay

Because undisturbed soft clay is inherently anisotropic owing to particle orientation in the deposition process, it experiences deformations due not only to variations in the magnitudes of the principal stresses but also to changes in their orientation with reference to the depositional plane. For test series I, results of monotonic loading tests on undisturbed Shanghai soft clay are shown in Fig. 4. The peak shear stress was reached in all tests and was taken as the undrained shear strength plotted with the principal stress direction.

It can be observed that the undrained shear strength decreases with increasing  $\alpha_\sigma$  and reaches its minimum value at approximately  $\alpha_\sigma = 45^\circ$ . Then, the undrained shear strength is slightly increased according to the increase in  $\alpha_\sigma$ . This undrained shear strength is dependent on major principal stress direction, similar to undisturbed

San Francisco clay by Lade and Kirkgard [16], London clay by Nishimura et al. [19], Wenzhou clay by Wang et al. [27], indicating clearly the inherent anisotropy of undisturbed Shanghai soft clay (see Fig. 4d).

The failure slope from monotonic tests can be plotted in  $p'$ - $q$  plane as a reference.  $M_{b=0.5}$  was obtained from the test MF00-1 of series I. The friction angle  $\phi_c = 42.1^\circ$  was calculated by SMP criterion according to Eq. (1) [32–34]. Then, the failure slope of  $M_{b=0}$  corresponding to the triaxial compression state and  $M_{b=1.0}$  corresponding to the triaxial extension state was calculated by Eqs. (2) and (3), respectively.

$$\frac{\tau_{\text{SMP}}}{\sigma_{\text{SMP}}} = \frac{2}{3} \sqrt{\left(\frac{\sigma_1 - \sigma_2}{2\sqrt{\sigma_1\sigma_2}}\right)^2 + \left(\frac{\sigma_2 - \sigma_3}{2\sqrt{\sigma_2\sigma_3}}\right)^2 + \left(\frac{\sigma_3 - \sigma_1}{2\sqrt{\sigma_3\sigma_1}}\right)^2} = \frac{2\sqrt{2}}{3} \tan \phi_c \quad (1)$$

$$M_{b=0} = \frac{6 \sin \phi_c}{3 - \sin \phi_c} \quad (2)$$

$$M_{b=1.0} = \frac{6 \sin \phi_c}{3 + \sin \phi_c} \quad (3)$$

#### 3.2 Variation of stress components

The stress trajectory of test series II and III is of the same shape, and only test series III is plotted in the deviatoric stress plane  $\tau_{z\theta} - (\sigma_z - \sigma_\theta)/2$ , shown in Fig. 5a–c, which is approximately a circle and almost identical to the designed stress path in Fig. 3b. The effective stress paths in  $p'$ - $q$  plane for test series II and series III are shown in Fig. 5d–f, in which the deviatoric stress  $q$  was maintained constant.

It is observed from Fig. 5d–f that the effective mean normal stress was reduced leading the soil to failure. Figure 5d–f also indicates that the number of cycles of rotation required to reach failure depends on both the  $b$  value and the magnitude of the deviatoric stress. For example, for the specimen subjected to a deviatoric stress of 60 kPa, 4 cycles of rotation bring it to failure under the condition of  $b = 0.5$  and  $b = 1.0$  but not for  $b = 0$ .

#### 3.3 Evolution of excess pore pressure

The excess pore pressures generated during principal stress rotation under various conditions are shown in Fig. 6. Although the deviatoric stress was maintained constant during the pure rotation test, the excess pore pressure buildup due to principal stress rotation alone was consistently observed. From the test results, the generation of excess pore pressure is dependent on the value of  $b$  and the magnitude of the deviatoric stress  $q$ . The rate of excess pore pressure

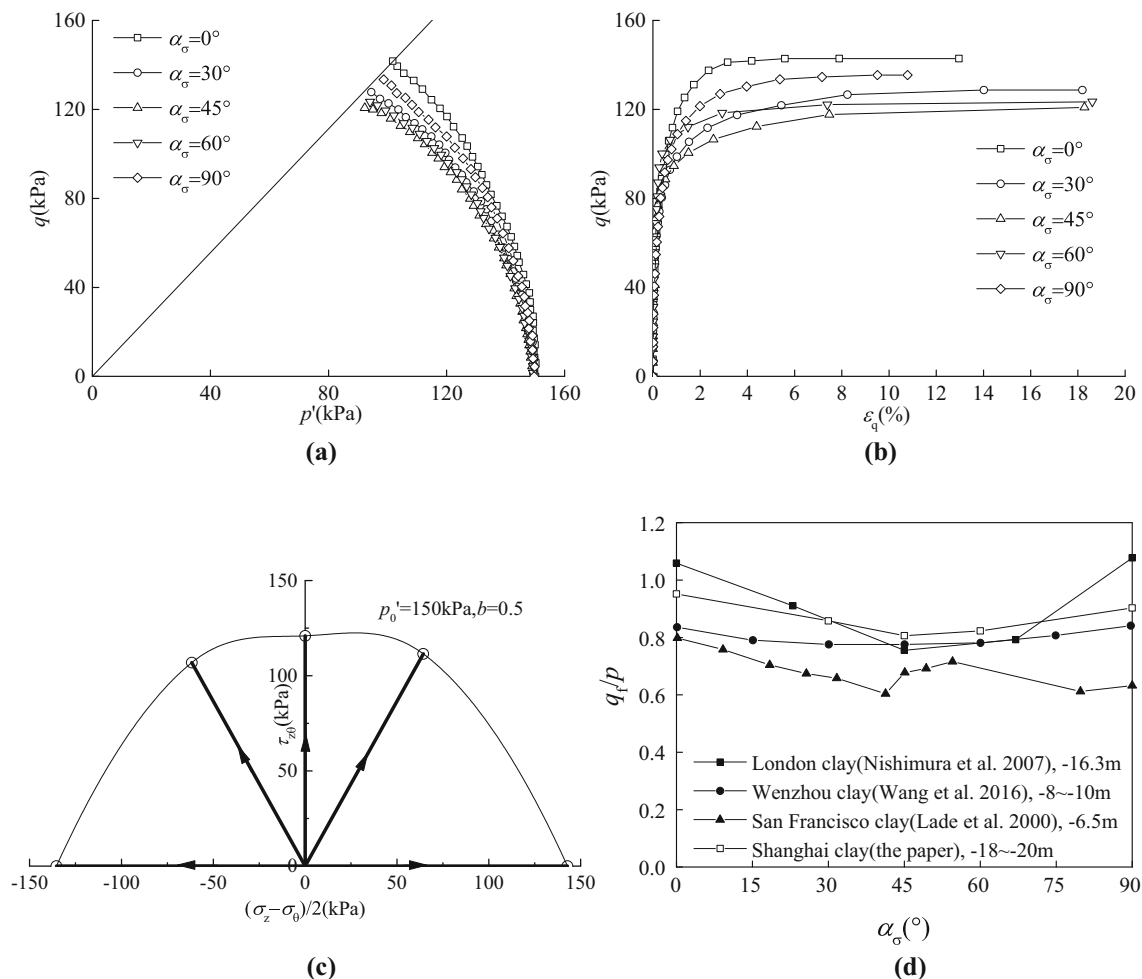


**Fig. 4** Results of monotonic loading tests on undisturbed Shanghai soft clay: **a** effective stress paths in  $p'$ - $q$  space; **b** stress-strain curves; **c** undrained shear strength variation under different principal stress directions

generation under the condition  $b = 0$  was slower than those under the conditions  $b = 0.5$  and  $b = 1.0$ , regardless of the deviatoric stress magnitude. This observation suggests that the relative magnitude of the intermediate principal stress plays an important role in principal stress rotation. Under otherwise identical conditions, the pore pressure generally increased more rapidly at the higher level of deviatoric stress, which suggests that the deviatoric stress magnitude also has a significant influence on the pore pressure response. These observations are in agreement with those observed in undrained tests of sand [18, 23, 28].

A better view of the variation of excess pore pressure in each cycle is plotted in Fig. 7, where the excess pore pressure ratio, defined as the ratio between the excess pore pressure and the initial mean effective stress, is a helpful representation of the undrained strength [28]. It is clear from Fig. 7 that the excess pore pressure decreases when  $\alpha_\sigma$  rotated from  $0^\circ$  to  $90^\circ$  and increases in the region from  $90^\circ$  to  $180^\circ$  except in the first cycle. A reasonable explanation for this observation can be the different resistance to

excess pore pressure exhibited in different directions of the soil, which can be related to the anisotropy of stress-dilatancy analysed by experiments of Ishihara and Towhata [15] and by the micromechanical model of Chang and Yin [5] and Yin and Chang [29]. The variation of  $(\sigma_z - \sigma_\theta)/2$  decreased first and then increased in a cycle brought about by this oscillation of excess pore pressure as shown in Fig. 7. The excess pore pressure also shows a dramatic change when  $\alpha_\sigma$  is near  $45^\circ$  and  $135^\circ$  owing to the lowest undrained shear strength at the specified weak fabric orientations, which in turn accelerate the generation of excess pore pressure, as shown in Fig. 5.

It is also observed from Fig. 7 that the excess pore pressure accumulates quickly at the primary stage, and the accumulation rate tends to decrease with increasing number of cycles. For example, at the first cycle of rotation, the value of the excess pore pressure ratio is 0.174, compared with 0.019 at the seventh cycle in the pure rotation stress path under the conditions of  $q = 30$  kPa and  $b = 0.5$ . Comparison between Fig. 7a and b suggests that the excess

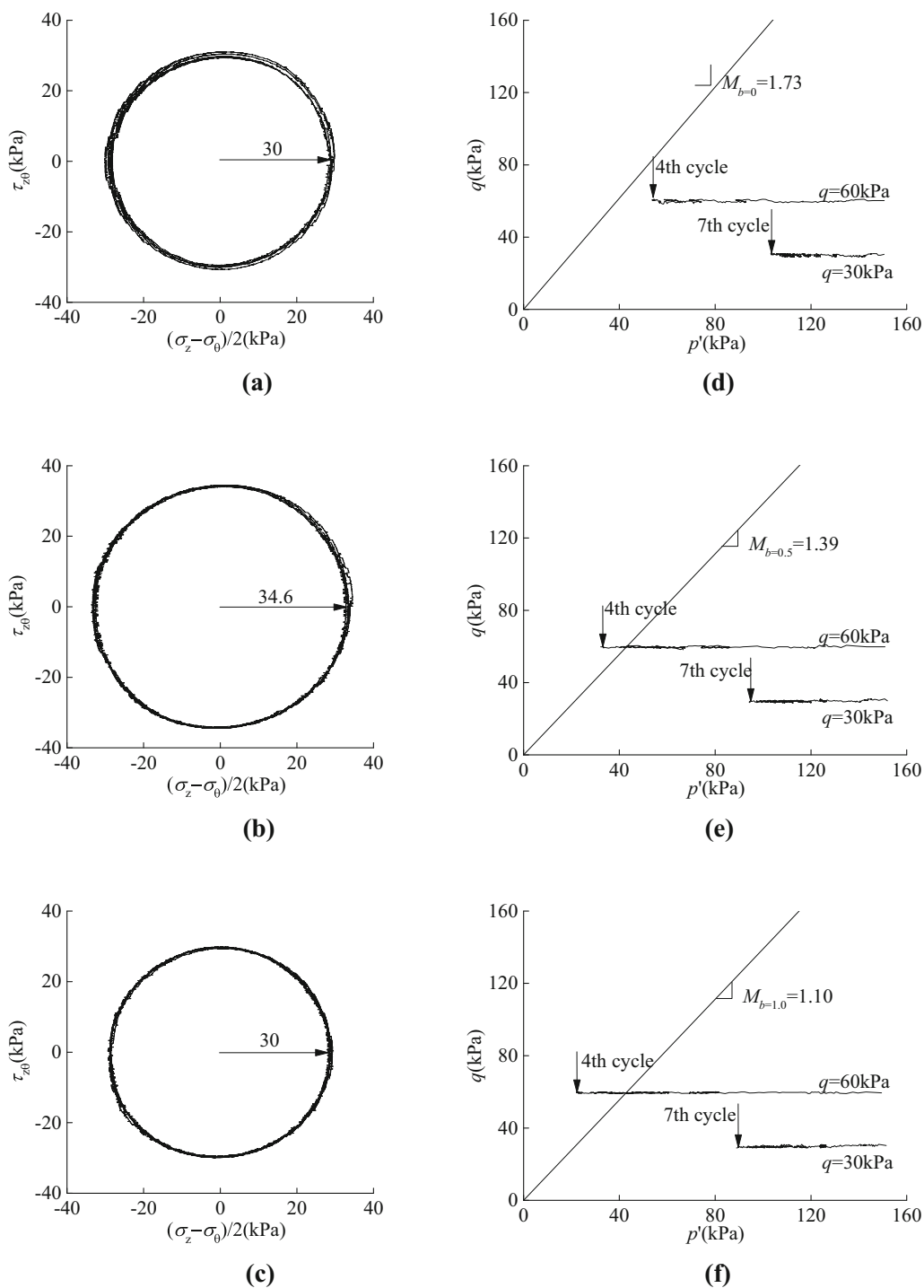


**Fig. 5** Stress trajectory in deviatoric stress space for test series III (a–c) and effective stress paths in  $p'$ - $q$  space for test series II and series III (d–f): **a**  $b = 0$ ; **b**  $b = 0.5$ ; **c**  $b = 1.0$ ; **d**  $b = 0$ ; **e**  $b = 0.5$ ; **f**  $b = 1.0$

pore pressure ratio fluctuated more in each cycle for higher deviatoric stress. For example, the fluctuation of the excess pore pressure ratio is 0.181 for the specimen subjected to a deviatoric stress of 60 kPa and  $b = 0.5$  and is 0.073 under the conditions of  $q = 30$  kPa and  $b = 0.5$  in the third cycle.

**3.4 Variation of strain components and strain paths**

The typical development of four normal strain components (contraction is defined positive in this paper) with the number of cycles for test series II and III under three cases of  $b$  is presented in Figs. 8 and 9. It is clear that although

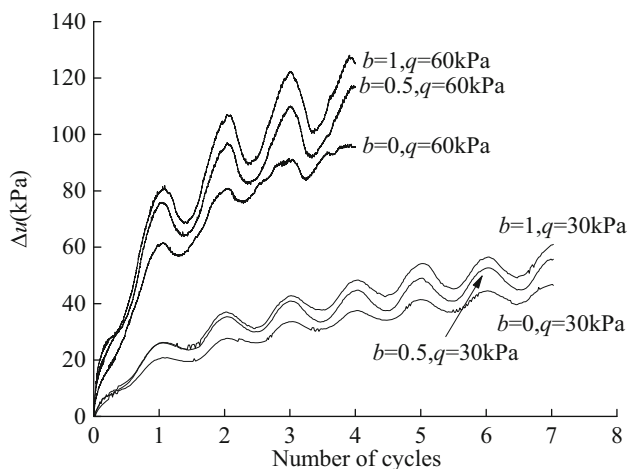


**Fig. 6** Excess pore pressures generated during pure principal stress rotation

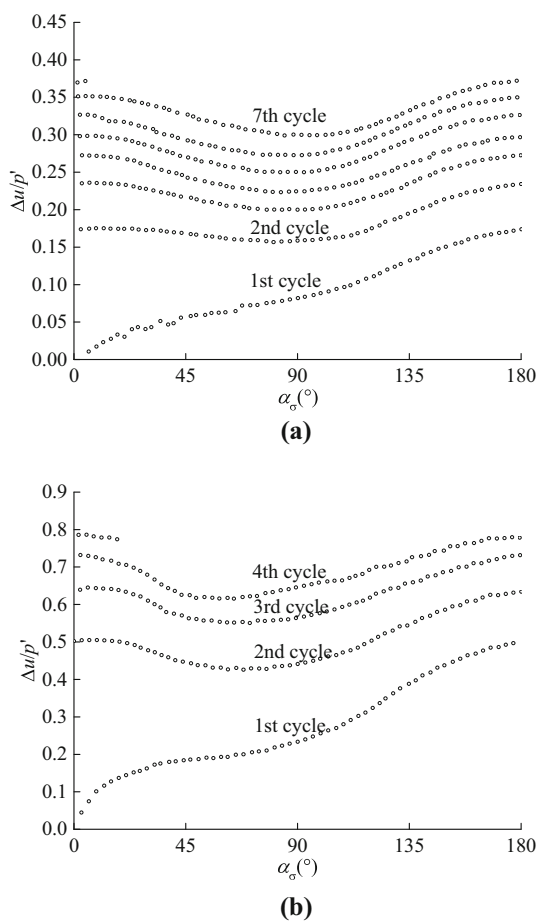


**Fig. 7** Variation of normalised excess pore pressure ratio with  $\alpha_\sigma$ : **a**  $q = 30$  kPa,  $b = 0.5$ ; **b**  $q = 60$  kPa,  $b = 0.5$

the magnitudes of deviatoric stress were maintained constant during the pure rotation test, apparent plastic strains were produced owing to principal stress rotation alone.

When  $\alpha_\sigma$  rotated starting from point B (Fig. 3b), the vertical strain  $\epsilon_z$  decreased, and the circumferential strain  $\epsilon_\theta$  increased, which coincides with the variation of the vertical stress and the circumferential stress, respectively. Owing to the inherent anisotropy due to particle orientation during the deposition process and the applied initial major principal stress direction along the  $z$ -axis before the principal stress rotation, the soil specimen has a lower contraction and higher dilatancy along the  $z$ -axis than those along the  $\theta$ -axis. As a result, a large dilative vertical strain and contractive circumferential strain are induced owing to the easier tendency. Meanwhile, it is clear that the shear strain  $\gamma_{z\theta}$  has a sinusoidal variation in a rotation cycle, which also coincides with the variation of the shear stress.

In Fig. 8, it can be found that the intermediate principal stress parameter  $b$  plays an important role in the development of the strain. The  $\epsilon_z$  and  $\epsilon_\theta$  change from contraction to dilatancy as  $b$  increased from 0 to 1.0. However, the radial strain  $\epsilon_r$  shows the opposite trends, varying from dilatancy to contraction as  $b$  increased from 0 to 0.5, and the contractive strain tends to develop under  $b = 1.0$ . Meanwhile, the variation of the shear strain has a similar pattern for all three values of  $b$  and shows only different amplitude. A reasonable explanation for the different evolution tendency of normal strains ( $\epsilon_z$ ,  $\epsilon_\theta$ , and  $\epsilon_r$ ) is that the value of  $b$  reflects the constraint in the radial direction. The low constraint under  $b = 0$  leads to the expansion of the radial strain, whereas  $\sigma_r$  becomes the major principal stress under  $b = 1.0$ . Finally, the contractive radial strain is induced owing to the easy contraction tendency caused by inherent anisotropy in the radial direction, and correspondingly,  $\epsilon_z$  and  $\epsilon_\theta$  changed from contraction to dilatancy.

Comparison between Figs. 8 and 9 also suggests that the deviatoric stress magnitude has a significant influence on the development of the strain. Under otherwise identical conditions, the strain components become gradually stable with the pure principal stress rotation at lower deviatoric stress  $q = 30$  kPa, as shown in Fig. 8, whereas it tends to gradually increase for tests under higher deviatoric stress  $q = 60$  kPa, shown in Fig. 9.

A better view of the behaviour influenced by the magnitude of deviatoric stress is provided by the strain paths in the deviatoric strain space for test series II and III, shown in Figs. 10 and 11. Clearly, the magnitudes of strains are accumulated by two different types with an increased number of cycles of rotation. For tests with lower deviatoric stress  $q = 30$  kPa, the strain envelope tends to stabilise gradually, but the position is kinematic. A drastic development of deformation can be observed in the pure rotation tests at higher deviatoric stress  $q = 60$  kPa, and the strain envelope is developed towards failure in a spiral manner with the principal stress rotation.

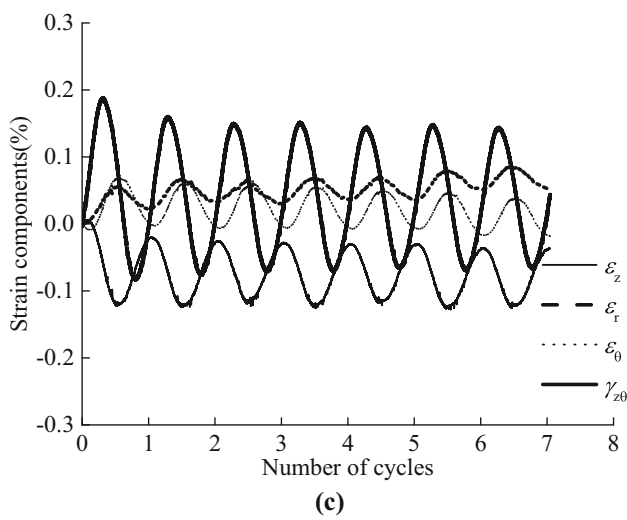
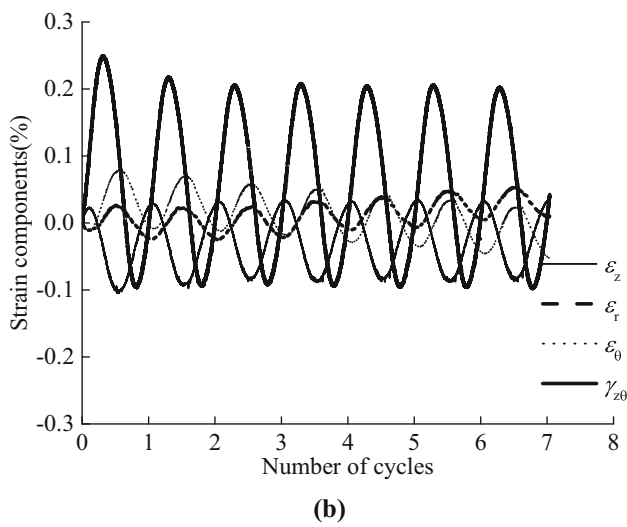
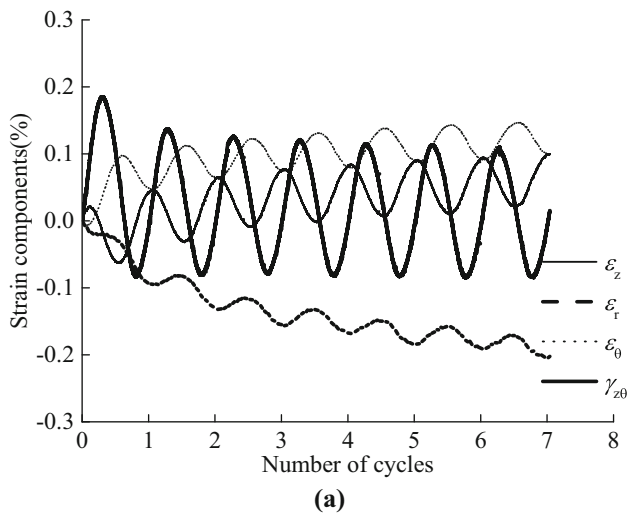


**Fig. 8** Variation of strain components during pure principal stress rotation for test series II: **a**  $b = 0$ ; **b**  $b = 0.5$ ; **c**  $b = 1.0$

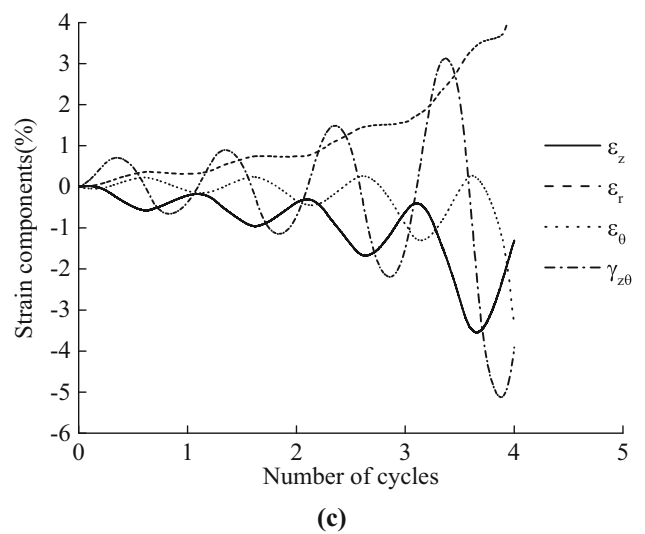
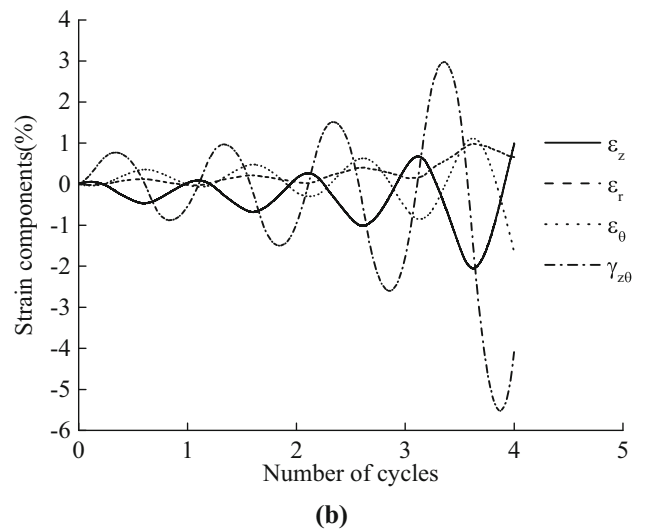
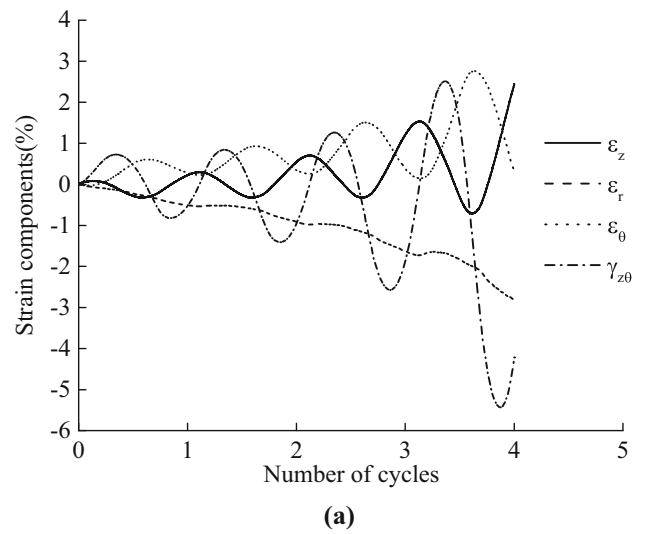
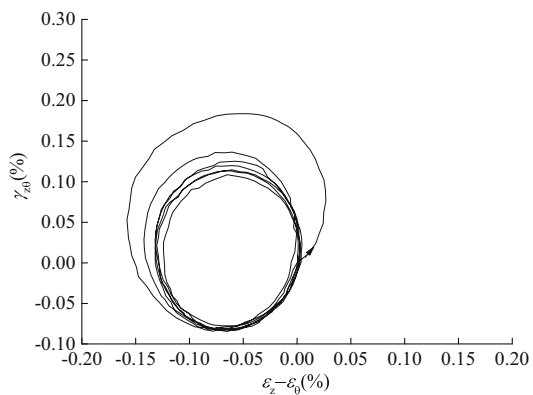
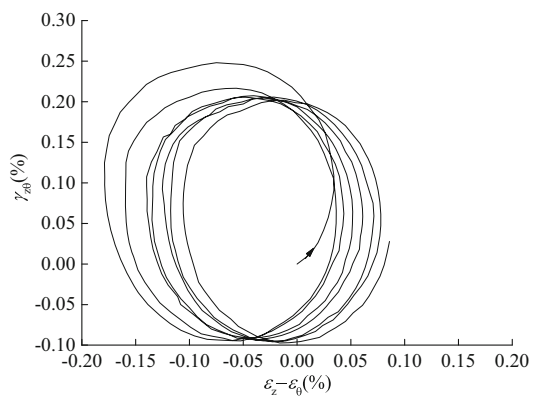


**Fig. 9** Variation of strain components during pure principal stress rotation for test series III: **a**  $b = 0$ ; **b**  $b = 0.5$ ; **c**  $b = 1.0$

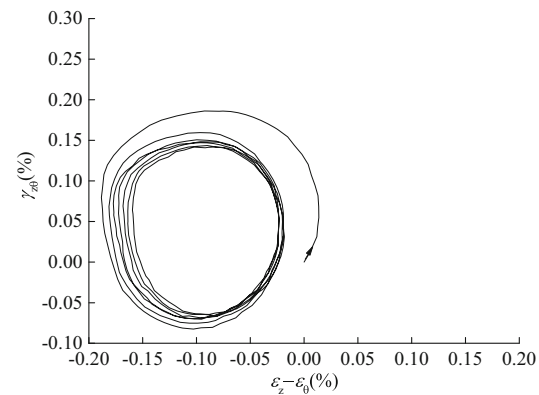




(a)



(b)

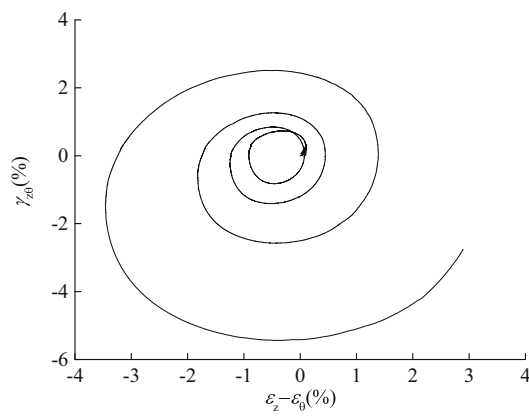


(c)

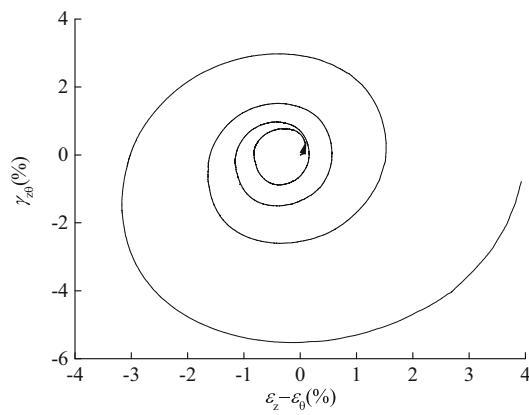
**Fig. 10** Strain paths in deviatoric strain space for test series II: **a**  $b = 0$ ; **b**  $b = 0.5$ ; **c**  $b = 1.0$

### 3.5 Stress–strain relationship and variation of stiffness

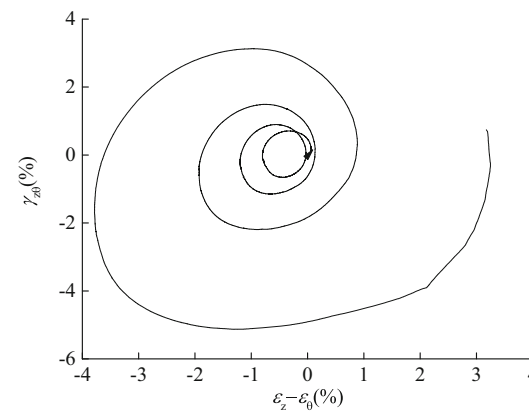
Figures 12 and 13 present the stress–strain relationship for test series II and III. It can be found that although the deviatoric stress is maintained constant during the pure rotation tests, the stress–strain curves are still hysteretic with plastic characteristics. It is notable that the deviatoric stress plays a significant role in the stress–strain



(a)



(b)



(c)

**Fig. 11** Strain paths in deviatoric strain space for test series III: **a**  $b = 0$ ; **b**  $b = 0.5$ ; **c**  $b = 1.0$

relationship in pure rotation tests. For tests with lower deviatoric stress  $q = 30$  kPa, the shear stress–strain relationship shows cyclic stability, and the hysteretic loops tend to become stable with increasing number of cycles, as shown in Fig. 12a–c. Meanwhile, the stress–strain curves shown in Fig. 12d–f are cyclic plastic creep, and the hysteretic loop size is maintained constant, but the position is

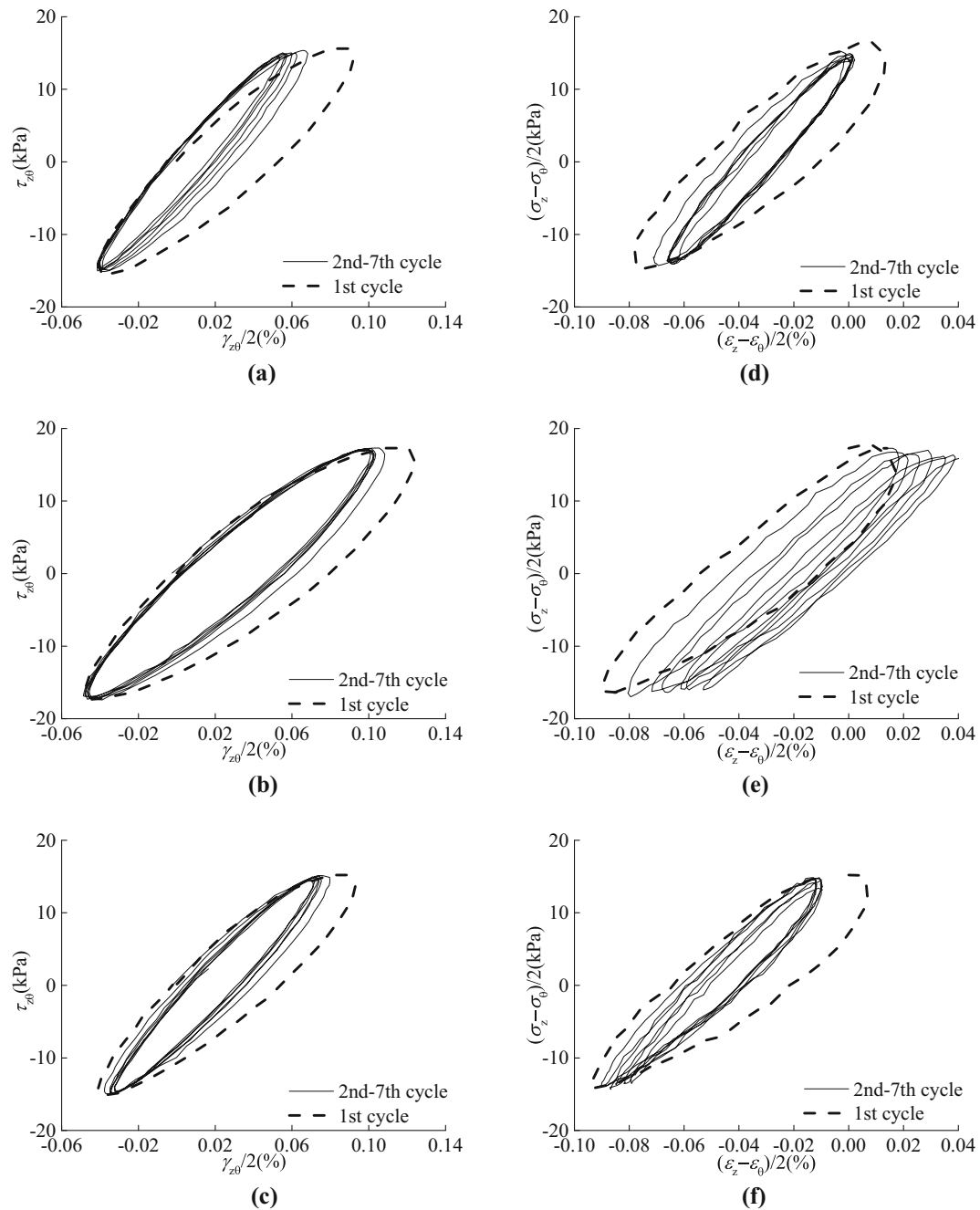


**Fig. 12** Shear stress–strain relationship (a–c) and normal differential stress–strain relationship (d–f) for test series II: **a, d**  $b = 0$ ; **b, e**  $b = 0.5$ ; **c, f**  $b = 1.0$

kinematic. However, as shown in Fig. 13 for tests with higher deviatoric stress  $q = 60$  kPa, the hysteretic loops appear unclosed, indicating the occurrence of plastic deformation due to the principal stress rotation alone, and tend to cyclic failure. The results show that there should be a threshold of deviatoric stress from cyclic mobility turned to cyclic degradation.

To achieve a better view of the importance of deviatoric stress, the stiffness is quantified and compared for two test series. Based mainly on the studies of Hill and Hutchinson

[12], Vardoulakis [26] and Desrues and Chambon [6], the secant modulus in the  $j$ th cycle of the shear stress–strain curve and normal differential stress–strain curve is defined as shear stiffness  $G_j^*$  and normal differential stiffness  $G_j$ , respectively. The stiffness is simply represented by the ratio between the  $j$ th cycle and the first cycle,  $G_j^*/G_1^*$  and  $G_j/G_1$ . The variation of stiffness ratio for different  $b$  values with the number of cycles is shown in Fig. 14. Comparison between Fig. 14a–b suggests that the variation of stiffness due to the change of the deviatoric stress magnitude shows

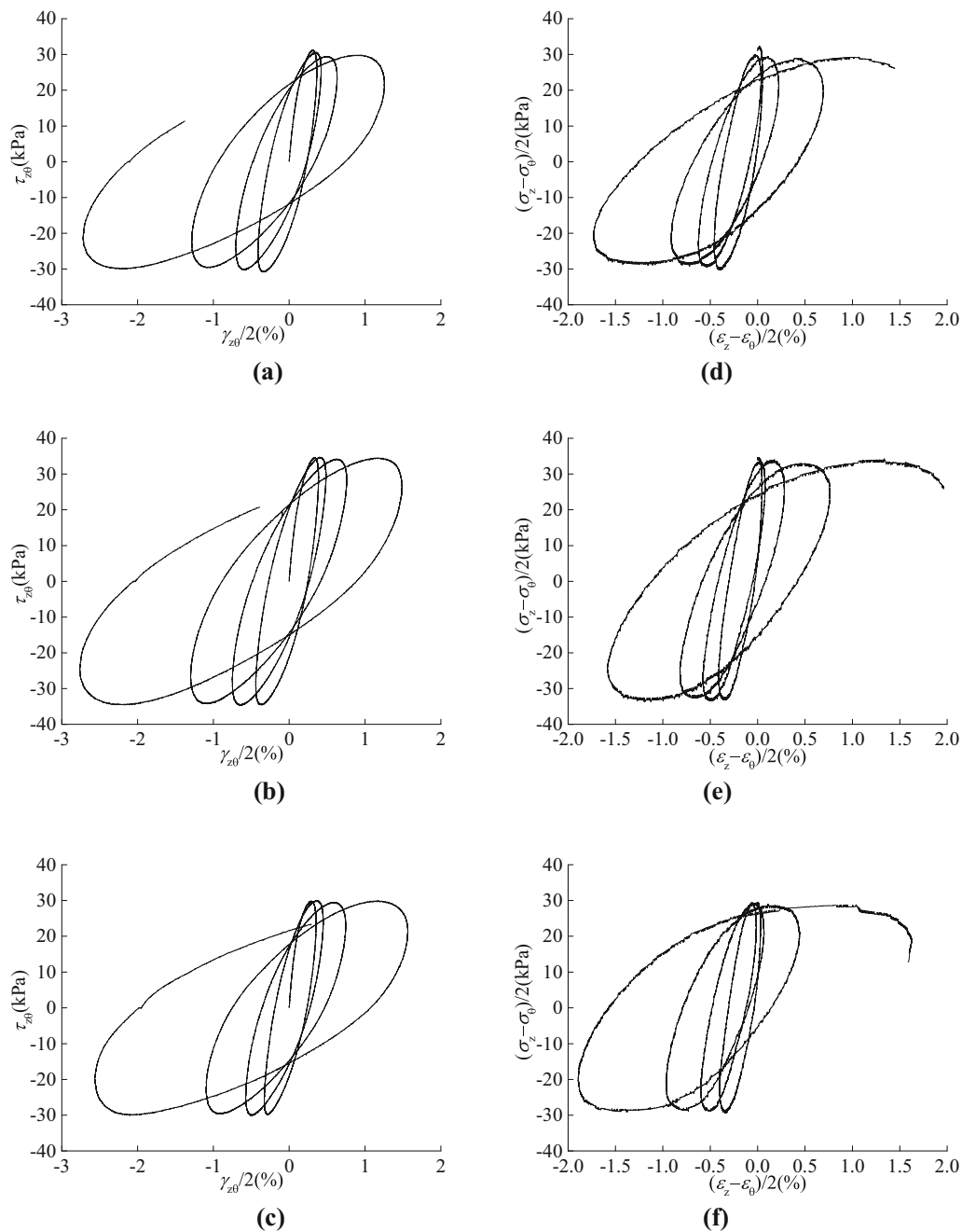


**Fig. 13** Shear stress–strain relationship (a–c) and normal differential stress–strain relationship (d–f) for test series III: a, d  $b = 0$ ; b, e  $b = 0.5$ ; c, f  $b = 1.0$

different patterns. For test series II, which were conducted at a lower deviatoric stress level, the stiffness experiences a slight hardening in the first 2 cycles and then remains approximately unchanged in subsequent cycles. For test series III, which were conducted at a higher level of  $q$ , the stiffness degradation is observed in cycles of principal stress rotation. By comparing the tests with different values of  $b$ , it can be seen that the effect due to the change of the  $b$  values is also considerable. The stiffness under the

conditions  $b = 0.5$  and  $b = 1.0$  is lower than that under the condition  $b = 0$ .

Based on Desrues and Chambon [6], it is incrementally isotropic case when the shear moduli  $G = G^*$  and the contrary is equivalent to say that the material is incrementally anisotropic. It is notable that the shear stiffness  $G_j^*$  and the normal differential stiffness  $G_j$  in cycles of principal stress rotation are unequal,  $G_j^* \neq G_j$ , indicating that the soil sample is incrementally anisotropic [6], which can be an

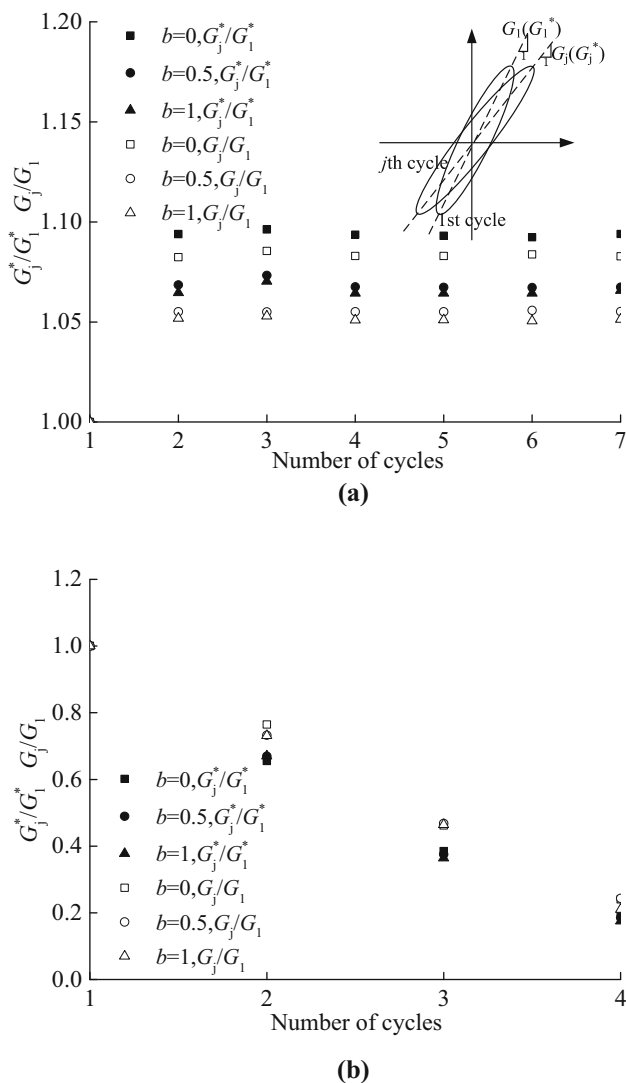


**Fig. 14** Variation of stiffness ratio for different  $b$  values: **a** series II; **b** series III

internal mechanism of induced non-coaxiality. This anisotropy reveals the results of Huang et al. [13] on the same Shanghai soft clay. Comparison between Fig. 14a–b also suggests that the shear stiffness is greater than the normal differential stiffness for test series II but not for test series III, which indicates that the stiffness degradation or stability is more pronounced by shear stress.

### 3.6 Non-coaxial behaviour

Roscoe et al. [21] were among the first to observe the non-coincidence between the principal stress direction and principal strain increment in simple shear tests. Experimental studies [9, 10, 15, 17] with HCA indicated that the plastic strain increment direction and the stress direction were non-coincident in principal stress rotation. This non-coincidence is

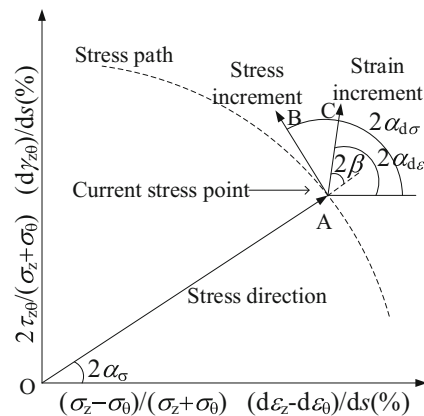


**Fig. 15** Stress path and non-coaxial behaviour between stress direction and strain increment direction

defined as non-coaxiality. However, it is difficult to separate the elastic strain increment from the total strain increment in the geotechnical unit test. Considering that the elastic strain components are inconsequential and can in fact be disregarded based mainly on the studies of Gutierrez et al. [10], the total strain increment will be replaced by the plastic strain increment in the following analysis. The stress path in the  $\tau_{z\theta} - (\sigma_z - \sigma_\theta)/2$  plane and the strain increment vector are shown in Fig. 15 where  $\alpha_\sigma$ ,  $\alpha_{d\sigma}$ , and  $\alpha_{d\epsilon}$  represent the inclination of the deposition direction with the major principal stress direction, major principal stress increment direction, and major principal strain increment direction, respectively. The non-coaxiality angle  $\beta$  is the direction between the strain increment and stress. The vectors **AB** ( $ds$ ) and **AC** are the stress increment and strain increment per unit stress increment (which imply flexibility in physics), respectively. They all can be calculated as follows:

$$\alpha_\sigma = \frac{1}{2} \arctan\left(\frac{2\tau_{z\theta}}{\sigma_z - \sigma_\theta}\right) \tag{4}$$

$$\alpha_{d\sigma} = \frac{1}{2} \arctan\left(\frac{2d\tau_{z\theta}}{d\sigma_z - d\sigma_\theta}\right) \tag{5}$$

$$\alpha_{d\epsilon} = \frac{1}{2} \arctan\left(\frac{d\gamma_{z\theta}}{d\epsilon_z - d\epsilon_\theta}\right) \tag{6}$$

$$\beta = \alpha_{d\epsilon} - \alpha_\sigma \tag{7}$$

$$abs(\mathbf{AB}) = ds = \sqrt{\left[d\left(\frac{\sigma_z - \sigma_\theta}{\sigma_z + \sigma_\theta}\right)\right]^2 + \left[d\left(\frac{2\tau_{z\theta}}{\sigma_z + \sigma_\theta}\right)\right]^2} \tag{8}$$

$$|\mathbf{AC}| = \frac{\sqrt{[d(\epsilon_z - \epsilon_\theta)]^2 + [d\gamma_{z\theta}]^2}}{ds} = \frac{d\epsilon_1 - d\epsilon_3}{ds} \tag{9}$$

If the direction of the strain increment vector coincides with the stress increment vector, it implies that the strain produced at each load increment is determined solely by

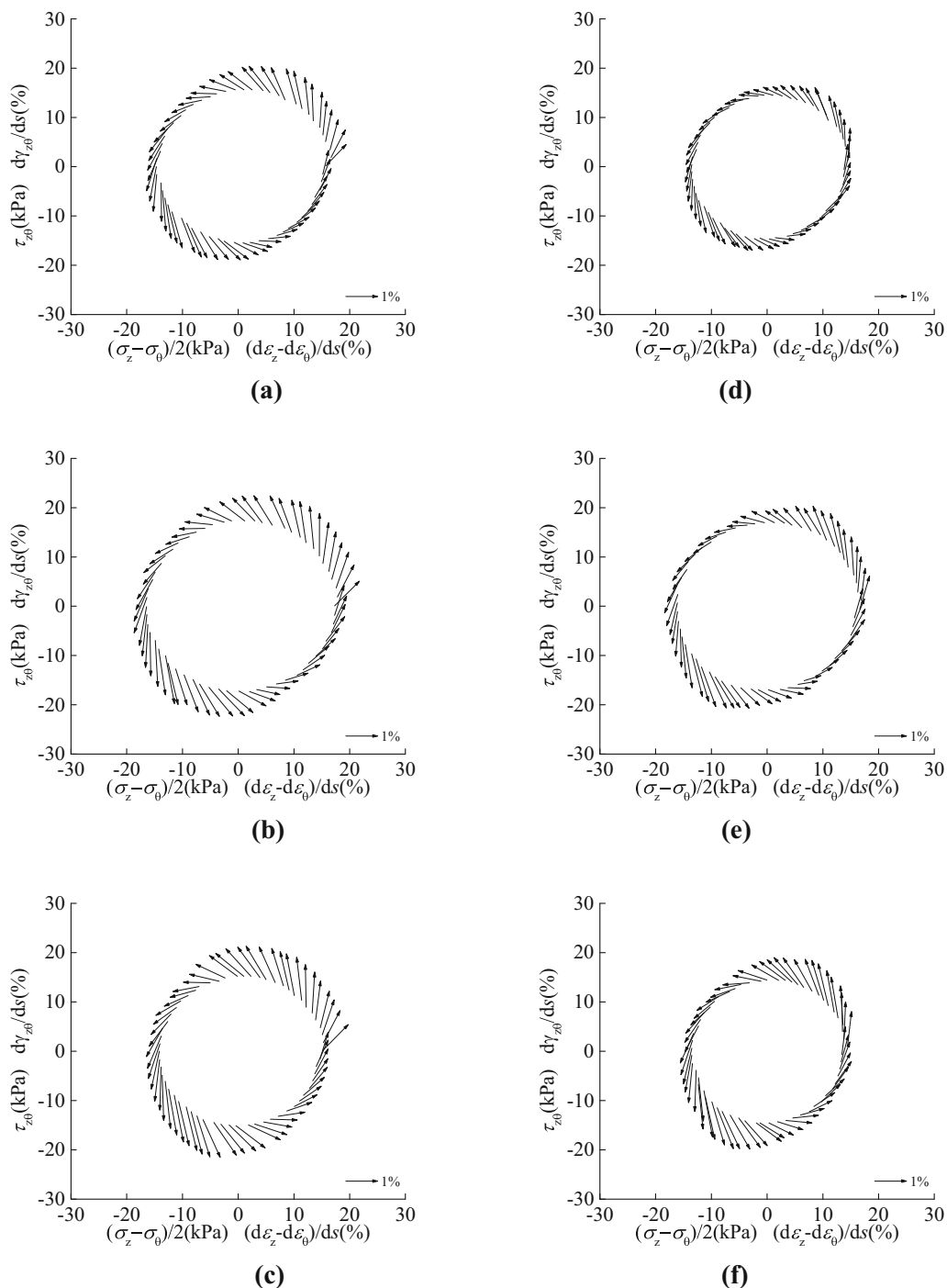


**Fig. 16** Stress path and strain increment vector in first cycle (a–c) and in seventh cycle (d–f) for series II: a, d  $b = 0$ ; b, e  $b = 0.5$ ; c, f  $b = 1.0$

changes in stress irrespective to the current state of stress. The stress–strain relationship will be similar to elastic behaviour, and the plastic deformation is induced by the stress rate [22]. Conversely, if the strain deformation is along with the stress vector irrespective to the stress increment, i.e.  $\beta = 0$ , then the plastic increment behaviour is referred to as the classic coaxial plastic rate.

Figures 16 and 17 present the stress paths and strain increment vectors for test series II and III. It can be found that the strain increment shows different levels of non-coaxiality under two deviatoric stresses, and the strain increment differs significantly in different stages. When  $\alpha_c$  rotated in ranges of  $[0^\circ, 45^\circ]$  and  $[90^\circ, 135^\circ]$  where the shear stress  $\tau_{z\theta}$  is increased, the deformation stiffness is

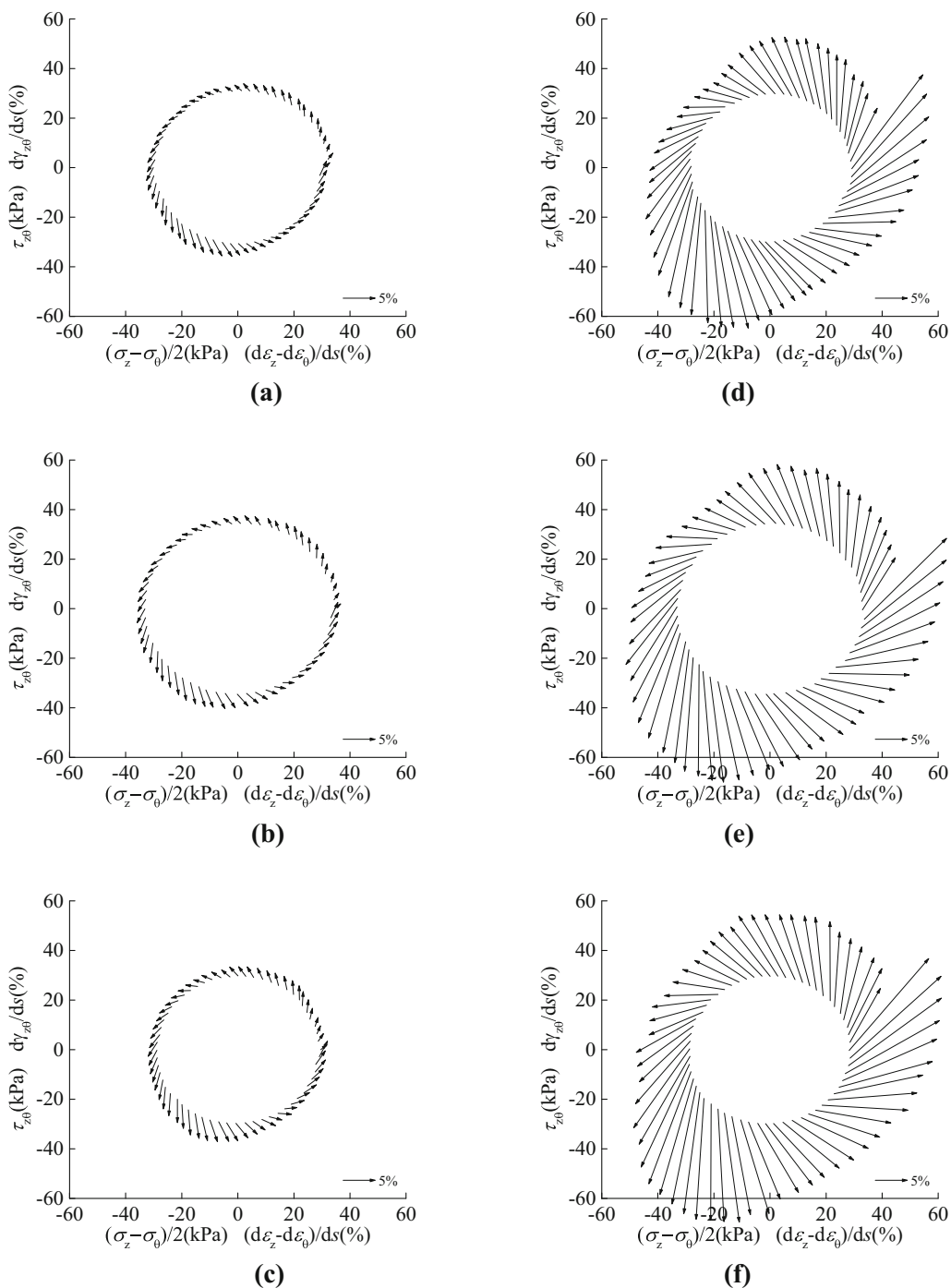


**Fig. 17** Stress path and strain increment vector in first cycle (a–c) and in fourth cycle (d–f) for series III: a, d  $b = 0$ ; b, e  $b = 0.5$ ; c, f  $b = 1.0$

small, the coaxial plastic rate is large, and the plastic effect caused by the stress rate is slight. In this case, the non-coaxiality angle is small; i.e. the clay behaves more like an ideal plastic material. However, when  $\tau_{z\theta}$  is decreased and  $\alpha_\sigma$  is in the ranges of  $[45^\circ, 90^\circ]$  and  $[135^\circ, 180^\circ]$ , the soil stiffness is larger, the coaxial plastic rate is smaller, and the plastic effect caused by the stress rate is significant. In this case, the non-coaxiality angle is bigger; i.e. the elastic-like

behaviour is induced in these ranges. Comparison between Figs. 16 and 17 suggests that the deformation stiffness is larger and the non-coaxiality is more important under lower deviatoric stress levels. This observation is in agreement with that observed in sand conducted under principal stress rotation by Gutierrez et al. [10].

To better reveal the correlation between non-coaxiality and soil stiffness and its anisotropy in cyclic loading,

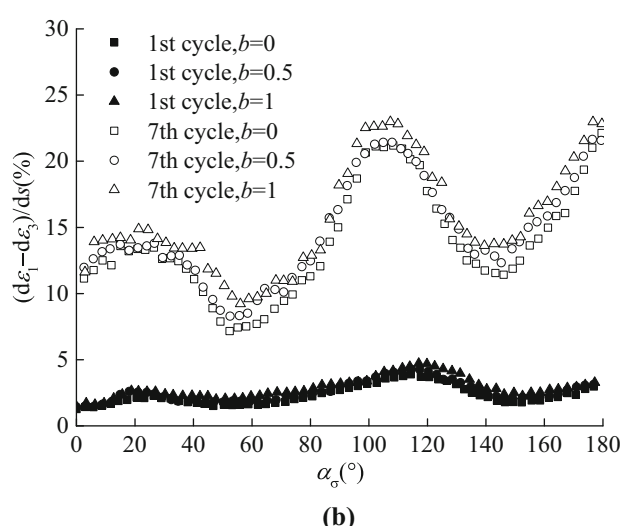
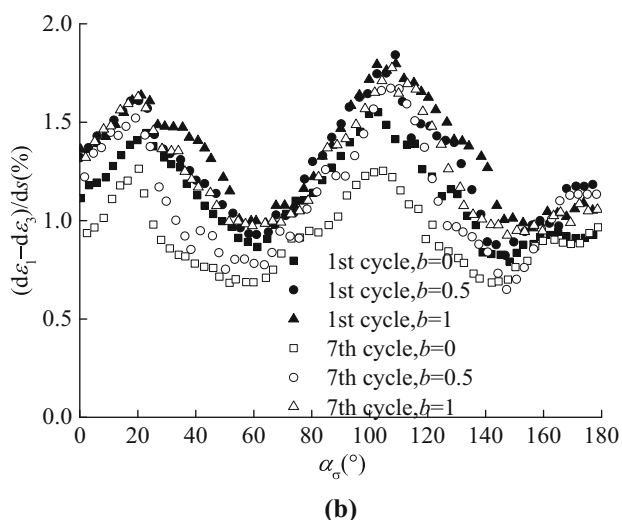
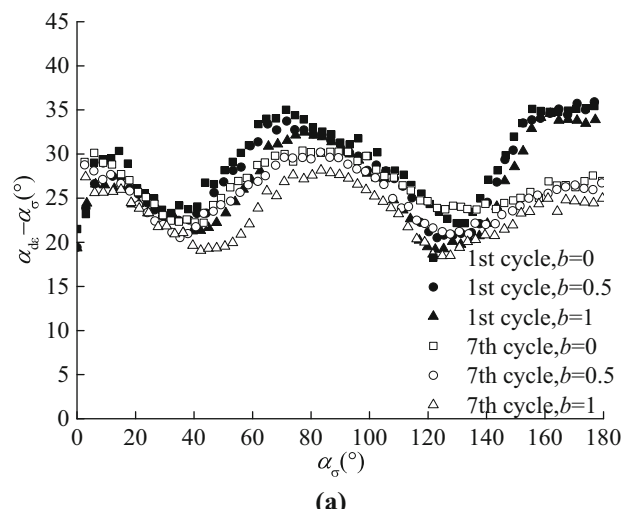
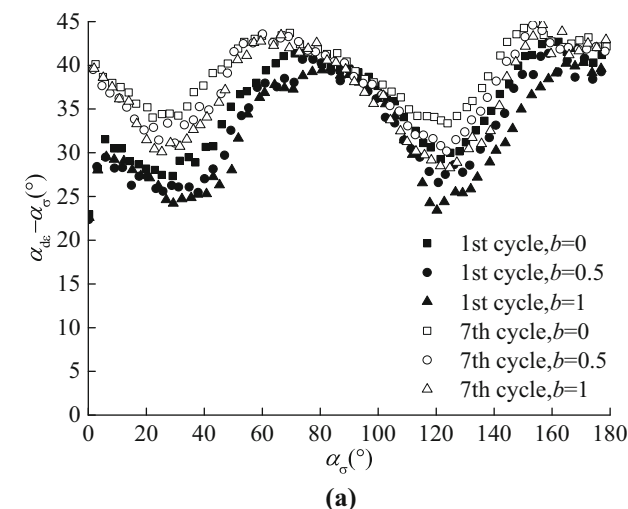


**Fig. 18** Variation of non-coaxiality angle and strain increment for series II: **a** non-coaxiality angle; **b** strain increment

**Fig. 19** Variation of non-coaxiality angle and strain increment for series III: **a** non-coaxiality angle; **b** strain increment

Figs. 18 and 19 illustrate the non-coaxiality angle and the magnitude of strain increment vector against the major principal stress direction for test series II and III. Considering Fig. 5, one can find that non-coaxiality is closely related to the strength anisotropy. When  $\alpha_\sigma$  rotated from  $0^\circ$  to  $45^\circ$  and  $90^\circ$  to  $135^\circ$ , the soil strength is decreased, the strain increment is increased (Figs. 18b and 19b), and the non-coaxiality is decreased (Figs. 18a and 19a). However, when  $\alpha_\sigma$  rotated in the ranges of  $45^\circ$ – $90^\circ$  and  $135^\circ$ – $180^\circ$ , the soil strength is increased, the strain increment is decreased, and the non-coaxiality is increased. Comparing Figs. 18 to 19 also suggests that the non-coaxiality increases owing to cyclic stiffness stability (Fig. 18b) at a lower deviatoric stress level, and the non-coaxiality is weakened because of cyclic degradation under the higher deviatoric stress level. There is no doubt that the cyclic evolution of non-coaxiality agrees with the segmentation

characteristics that the non-coaxiality depends on the stiffness variation in one cycle. The non-coaxiality variation under deviatoric stress level depends on stiffness, and the stiffness degradation or stability is also consistent.

### 4 Conclusions

This paper investigated the undrained deformation behaviour of soft clay under the effects of pure principal stress rotation using a hollow cylinder apparatus. Monotonic loading tests were first carried out to investigate the inherent anisotropy of undisturbed Shanghai soft clay. Pure rotation stress path tests were then conducted in which the deviatoric stress, the mean effective stress, and the intermediate principal stress parameter remained constant, whereas only the principal stress direction was rotated

continuously and cyclically. The stiffness degradation and non-coaxiality were observed particularly, based on which the dependence between the non-coaxiality and the strength anisotropy was discussed. The major experimental conclusions are summarised as follows:

1. The excess pore pressure was accumulated owing to the rotation of principal stress direction, even though the deviatoric stress was maintained constant during the pure rotation test. The intermediate principal stress parameter  $b$  and the magnitude of deviatoric stress had a significant effect on the response of excess pore pressure. The rate of excess pore pressure generation was increased with increasing  $b$ , and the larger the deviatoric stress, the faster the pore pressure buildup.
2. Although the deviatoric stress was maintained constant during principal stress rotation, the stress–strain curves showed hysteretic and plastic characteristics. The stress–strain characteristics were significantly affected by the deviatoric stress. At higher deviatoric stress levels, the stiffness degrades. However, under lower deviatoric stress levels the stiffness experienced a slight hardening in the first 2 cycles but remained approximately unchanged in subsequent cycles. Furthermore, the stiffness is decreased with increasing  $b$  value.
3. Plastic deformation was induced owing to principal stress rotation alone. The  $b$  value and the magnitude of deviatoric stress had a significant effect on the deformation characteristics. The strain envelope was

kinematic in position and tended to stabilise with the cyclic stiffness stability at lower deviatoric stress levels. However, with the cyclic stiffness degradation under higher deviatoric stress, the strain envelope in the deviatoric strain space developed towards failure in an open spiral manner.

4. Apparent non-coaxiality was observed during pure principal stress rotation. The non-coaxiality showed segmentation characteristics. Shear stress–strain stiffness and normal differential stress–strain curves were observed. The difference between them indicated incremental anisotropy, which was an internal mechanism of non-coaxiality. With cyclic stiffness stability at lower deviatoric stress levels, the non-coaxiality tended to increase. Conversely, with cyclic stiffness degradation at a higher deviatoric stress level, the non-coaxiality tended to weaken.

In future work, tests with more or high number of cycles will be carried out for long-term behaviour of cyclic degradation and non-coaxiality.

**Acknowledgements** The study is financially supported by the National Natural Science Foundation of China (Grant Nos. 41272291, 41372285, 51238009, 51578413 and 51579179).

**Appendix: Equations used to calculate the stress and strain parameters**

See Table 3.

**Table 3** Test parameter calculation

	Stress	Strain
Vertical	$\sigma_z = \frac{W}{\pi(r_o^2 - r_i^2)} + \frac{P_o r_o^2 - P_i r_i^2}{r_o^2 - r_i^2}$	$\epsilon_z = \frac{z}{H}$
Radial	$\sigma_r = \frac{P_o r_o + P_i r_i}{r_o + r_i}$	$\epsilon_r = -\frac{u_o - u_i}{r_o - r_i}$
Circumferential	$\sigma_\theta = \frac{P_o r_o - P_i r_i}{r_o - r_i}$	$\epsilon_\theta = -\frac{u_o + u_i}{r_o + r_i}$
Shear	$\tau_{z\theta} = \frac{3T}{2\pi(r_o^3 - r_i^3)}$	$\gamma_{z\theta} = \frac{2\theta(r_o^3 - r_i^3)}{3H(r_o^2 - r_i^2)}$
Major principal	$\sigma_1 = \frac{\sigma_z + \sigma_\theta}{2} + \sqrt{\left(\frac{\sigma_z - \sigma_\theta}{2}\right)^2 + \tau_{z\theta}^2}$	$\epsilon_1 = \frac{\epsilon_z + \epsilon_\theta}{2} + \sqrt{\left(\frac{\epsilon_z - \epsilon_\theta}{2}\right)^2 + \left(\frac{\gamma_{z\theta}}{2}\right)^2}$
Intermediate principal	$\sigma_2 = \sigma_r$	$\epsilon_2 = \epsilon_r$
Minor principal	$\sigma_3 = \frac{\sigma_z + \sigma_\theta}{2} - \sqrt{\left(\frac{\sigma_z - \sigma_\theta}{2}\right)^2 + \tau_{z\theta}^2}$	$\epsilon_3 = \frac{\epsilon_z + \epsilon_\theta}{2} - \sqrt{\left(\frac{\epsilon_z - \epsilon_\theta}{2}\right)^2 + \left(\frac{\gamma_{z\theta}}{2}\right)^2}$
Volumetric	$p' = \frac{\sigma'_1 + \sigma'_2 + \sigma'_3}{3} = \frac{\sigma_1 + \sigma_2 + \sigma_3}{3} - u$	$\epsilon_v = \epsilon_1 + \epsilon_2 + \epsilon_3$
Deviatoric	$q = \sqrt{\frac{1}{2}[(\sigma_1 - \sigma_2)^2 + (\sigma_2 - \sigma_3)^2 + (\sigma_3 - \sigma_1)^2]}$	$\epsilon_q = \sqrt{\frac{2}{9}[(\epsilon_1 - \epsilon_2)^2 + (\epsilon_2 - \epsilon_3)^2 + (\epsilon_3 - \epsilon_1)^2]}$



## References

1. Akagi H, Saitoh J (1994) Dilatancy characteristics of clayey soil under principal axes rotation. Conference on Pre-Failure Deformation Characteristics of Geomaterial 311–314
2. Akagi H, Yamamoto H (1997) Stress-dilatancy relation of undisturbed clay under principal axes rotation. Conference on Deformation and progressive failure in Geomechanics 211–216
3. Arthur JRF, del Rodriguez CJI, Dunstan T, Chua KS (1980) Principal stress rotation: a missing parameter. *J Geotech Eng Div* 106(4):419–433
4. Cai Y, Sun Q, Guo L, Juang CH, Wang J (2015) Permanent deformation characteristics of saturated sand under cyclic loading. *Can Geotech J* 52(6):795–807. doi:[10.1139/cgj-2014-0341](https://doi.org/10.1139/cgj-2014-0341)
5. Chang CS, Yin Z-Y (2009) Modeling stress-dilatancy for sand under compression and extension loading conditions. *J Eng Mech* 136(6):777–786
6. Desrues J, Chambon R (2002) Shear band analysis and shear moduli calibration. *Int J Solids Struct* 39(13):3757–3776
7. Guo L, Chen J, Wang J, Cai Y, Deng P (2016) Influences of stress magnitude and loading frequency on cyclic behavior of K0-consolidated marine clay involving principal stress rotation. *Soil Dyn Earthq Eng* 84:94–107. doi:[10.1016/j.soildyn.2016.01.024](https://doi.org/10.1016/j.soildyn.2016.01.024)
8. Guo L, Wang J, Cai Y, Liu H, Gao Y, Sun H (2013) Undrained deformation behavior of saturated soft clay under long-term cyclic loading. *Soil Dyn Earthq Eng* 50:28–37. doi:[10.1016/j.soildyn.2013.01.029](https://doi.org/10.1016/j.soildyn.2013.01.029)
9. Gutierrez M, Ishihara K (2000) Non-coaxiality and energy dissipation in granular materials. *Soils Found* 40(2):49–59
10. Gutierrez M, Ishihara K, Towhata I (1991) Flow theory for sand during rotation of principal stress direction. *Soils Found* 31(4):121–132
11. Hight D, Gens A, Symes M (1983) The development of a new hollow cylinder apparatus for investigating the effects of principal stress rotation in soils. *Geotechnique* 33(4):355–383
12. Hill R, Hutchinson J (1975) Bifurcation phenomena in the plane tension test. *J Mech Phys Solids* 23(4):239–264
13. Huang M, Liu Y, Sheng D (2011) Simulation of yielding and stress–strain behavior of shanghai soft clay. *Comput Geotech* 38(3):341–353
14. Ishihara K (1983) Soil response in cyclic loading induced by earthquakes, traffic and waves. Proceedings of the 7th Asian Regional Conference on Soil Mechanics and Foundation Engineering 42–66
15. Ishihara K, Towhata I (1983) Sand response to cyclic rotation of principal stress directions as induced by wave loads. *Soils Found* 23(4):11–26
16. Lade PV, Kirkgard MM (2000) Effects of stress rotation and changes of b-values on cross-anisotropic behavior of natural, K0-consolidated soft clay. *Soils Found* 40(6):93–105
17. Miura K, Miura S, Toki S (1986) Deformation behavior of anisotropic dense sand under principal stress axes rotation. *Soils Found* 26(1):36–52
18. Nakata Y, Hyodo M, Murata H, Yasufuku N (1998) Flow deformation of sands subjected to principal stress rotation. *Soils Found* 38(2):115–128
19. Nishimura S, Minh N, Jardine R (2007) Shear strength anisotropy of natural London clay. *Geotechnique* 57(1):49–62
20. Qian JG, Wang YG, Yin ZY, Huang MS (2016) Experimental identification of plastic shakedown behavior of saturated clay subjected to traffic loading with principal stress rotation. *Eng Geol* 214:29–42
21. Roscoe K, Bassett R, Cole E (1967) Principal axes observed during simple shear of a sand. Proceedings of the Geotechnical Conference 231–237
22. Rudnicki JW, Rice JR (1975) Conditions for the localization of deformation in pressure-sensitive dilatant materials. *J Mech Phys Solids* 23(6):371–394
23. Shibuya S, Hight D, Symes M (1984) sand response to cyclic rotation of principal stress directions as induced by wave loads. *Soils Found* 24(3):107–110
24. Symes M, Gens A, Hight D (1984) Undrained anisotropy and principal stress rotation in saturated sand. *Geotechnique* 34(1):11–27
25. Tong Z, Zhang J, Yu Y, Zhang G (2010) Drained deformation behavior of anisotropic sands during cyclic rotation of principal stress axes. *J Geotech Geoenviron Eng* 136(11):1509–1518
26. Vardoulakis I (1980) Shear band inclination and shear modulus of sand in biaxial tests. *Int J Numer Anal Meth Geomech* 4(2):103–119
27. Wang YK, Guo L, Gao YF, Qiu Y, Hu XQ, Zhang Y (2016) Anisotropic drained deformation behavior and shear strength of natural soft marine clay. *Mar Georesour Geotechnol* 34(5):493–502
28. Yang Z, Li X, Yang J (2007) Undrained anisotropy and rotational shear in granular soil. *Geotechnique* 57(4):371–384
29. Yin Z-Y, Chang CS (2013) Stress–dilatancy behavior for sand under loading and unloading conditions. *Int J Numer Anal Meth Geomech* 37(8):855–870
30. Yin Z-Y, Chang CS, Hicher PY (2010) Micromechanical modelling for effect of inherent anisotropy on cyclic behaviour of sand. *Int J Solids Struct* 47(14–15):1933–1951
31. Yin Z-Y, Xu Q, Chang CS (2013) Modeling cyclic behavior of clay by micromechanical approach. *ASCE J Eng Mech* 139(9):1305–1309
32. Yao YP, Lu DC, Zhou AN (2004) Generalized non-linear strength theory and transformed stress space. *Sci China Ser E* 47(6):691–709
33. Yao YP, Sun DA, Matsuoka H (2008) A unified constitutive model for both clay and sand with hardening parameter independent on stress path. *Comput Geotech* 35(2):210–222
34. Yao YP, Hou W, Zhou AN (2009) UH model: three-dimensional unified hardening model for overconsolidated clays. *Geotechnique* 59(5):451–469
35. Zhou J, Yan J, Liu Z, Gong X (2014) Undrained anisotropy and non-coaxial behavior of clayey soil under principal stress rotation. *J Zhejiang Univ-Sci A (Appl Phys Eng)* 15(4):241–254
36. Zhou J, Yan J, Xu C, Gong X (2013) Influence of intermediate principal stress on undrained behavior of intact clay under pure principal stress rotation. *Math Probl Eng* 2013:1–10. doi:[10.1155/2013/950143](https://doi.org/10.1155/2013/950143)